RESEARCH ARTICLE

CARBON ENERGY WILEY

Vacuum-free lamination via controlled polymer adhesion for selective photogeneration and photodetection

Min Soo Kim[1] | Jihyun Lim[1] | Woongsik Jang[2] | Dong Hwan Wang[1,2]

[1]Department of Intelligent Semiconductor Engineering, Chung-Ang University, Seoul, Republic of Korea

[2]School of Integrative Engineering, Chung-Ang University, Seoul, Republic of Korea

Correspondence
Dong Hwan Wang, School of Integrative Engineering, Chung-Ang University, 84 Heukseok-ro, Dongjak -gu, Seoul 06974, Republic of Korea.
Email: king0401@cau.ac.kr

Abstract

This study attempts to develop a reproducible thin-film formation technique called vacuum-free (VF) lamination, which transfers thin films using elastomeric polymer-based laminating mediators. Precisely, by controlling the interface characteristics of the mediator based on the work of adhesion, VF lamination is successfully performed for various thicknesses (from 20 to 240 nm) of a conjugated photoactive material composed of poly[(2,6-(4,8-bis (5-(2-ethylhexyl-3-fluoro)thiophen-2-yl)-benzo[1,2-b:4,5-b′]dithiophene))-alt-(5,5-(1′,3′-di-2-thienyl-5′,7′-bis(2-ethylhexyl)benzo[1′,2′-c:4′,5′-c′]dithiophene-4,8-dione)] (a polymer donor) and 2,2′-((2Z,2′Z)-((12,13-bis(2-butyloctyl)-3, 9-diundecyl-12,13-dihydro-[1,2,5]thiadiazolo[3,4-e]thieno[2′′,3′′:4′,5′]thieno [2′,3′:4,5]pyrrolo[3,2-g]thieno[2′,3′:4,5]thieno[3,2-b]indole-2,10-diyl)bis (methanylylidene))bis(5,6-difluoro-3-oxo-2,3-dihydro-1H-indene-2,1-diylidene)) dimalononitrile (a nonfullerene acceptor). Interestingly, the organic photo-voltaic and photodetecting applications, prepared by the VF lamination process, showed superior performance compared to those of devices prepared by conventional spin-coating. This is due to the overturned surface morphology, which led to enhanced charge transport ability and blocking of the externally injected charge. Thus, the reproducible VF lamination process, exploiting an adhesion-based elastomeric polymer mediator, is a promising thin-film formation technique for developing efficient next-generation organic opto-electronic materials consistent with the solution process.

KEYWORDS
conjugated, nonfullerene acceptor, photodetectors, photovoltaics, polymer, vacuum-free lamination

1 | INTRODUCTION

Solution-processable conjugated organic semiconductor materials have attracted huge research interest because of their enormous potential for use in manufacturing processes owing to characteristics such as ease of printing, large scalability, flexibility, and cost-effectiveness.[1–6] Recently, it was reported that with the development of new, novel polymer donors and non-fullerene acceptors (NFAs), the power conversion

efficiency (PCE) of single-junction organic photovoltaics (PVs) exceeded 19% and the detectivity of organic photodetectors (PDs) increased beyond 10^{14} Jones.[7–10] In addition to the realization of these new materials, the manipulation of micro-morphology based on phase separation is key to enhancing performance. As a result, numerous strategies have been developed, such as adjusting the solvents (and additives), introducing a guest component, controlling the ratio of donors and acceptors, and coating processes.[11–14]

Although blends containing donors and acceptors are well controlled by the above-listed strategies, when different surface energies exist between the donor and the acceptor, phase separation occurs during the film formation process, especially in the thick photoactive layer. Moreover, the small-molecular acceptor materials settle at the bottom and the polymer donor tends to move to the surface, which can negatively affect the specific vertical device structure.[15,16]

Accordingly, the development of a new thin-film formation process to control the morphology of films is a crucial challenge in the field of solution-processed conjugated organic electronic devices.[17–20] Therefore, to achieve a desirable film surface morphology with a well-distributed donor and acceptor phase in the vertical structure, we developed a vacuum-free (VF) lamination process, in which the target material is dry-transferred onto the substrates without the vacuum process. In particular, using this approach, the surface morphology can be controlled based on the reversal effect of thin films regardless of the type or thickness of the material.[21]

To realize the reproducible VF lamination process, we synthesized adhesion-controlled polyurethane acrylate (PUA)-based transfer mediators considering the surface energy between the mediator and the target material. Accordingly, we successfully carried out the VF lamination process on photoactive layers composed of poly[(2,6-(4, 8-bis(5-(2-ethylhexyl-3-fluoro)thiophen-2-yl)-benzo[1,2-b:4,5-b′]dithiophene))-alt-(5,5-(1′,3′-di-2-thienyl-5′,7′-bis(2-ethylhexyl)benzo[1′,2′-c:4′,5′-c′]dithiophene-4,8-dione)] (PM6) and 2,2′-((2Z,2′Z)-((12,13-bis(2-butyloctyl)-3, 9-diundecyl-12,13-dihydro-[1,2,5]thiadiazolo[3,4-e]thieno [2′′,3′′:4′,5′]thieno[2′,3′:4,5]pyrrolo[3,2-g]thieno[2′,3′:4,5] thieno[3,2-b]indole-2,10-diyl)bis(methanylylidene))bis(5,6-difluoro-3-oxo-2,3-dihydro-1H-indene-2,1-diylidene)) dimalononitrile (BTP-4F-12) with various thicknesses using adhesion-optimized PUA mediators.

Among the devices with various thicknesses of VF-laminated PM6:BTP-4F-12, we selected a specific thickness for PV and PD applications. In addition, we confirmed the superiority of the VF lamination–processed devices compared to spin-coated devices through optical, electrical, morphological, and stability analyses.

2 | EXPERIMENTAL SECTION

2.1 | Preparation of materials

Aliphatic urethane diacrylate (UA) oligomer (Ebecryl 9270; SK Cytec), 1-hydroxycyclohhexyl phenyl ketone (HCPK; Sigma–Aldrich), 2-hydroxyethyl acrylate (HEA; Sigma–Aldrich), 2,2,2,-trifluoro methacrylate (TFMA; Sigma–Aldrich), and perfluoropolyether (PFPE; SKChems) were used for the fabrication of the VF lamination mediator. Poly(3,4-ethylenedioxythiophene) poly(styrenesulfonate) (PEDOT:PSS) was used as a hole transport material and N,N'-bis{3-[3-(dimethylamino) propylamino]propyl}perylene-3,4,9,10-tetracarboxylic diimide (PDINN) was used as an electron transport material, and these were purchased from Heraeus and 1-Material, respectively. PM6 and BTP-4F-12 were purchased from Brilliant Matters.

2.2 | Synthesis of VF lamination mediators

The normal PUA solution was synthesized using 9.5 g of UA oligomer and 0.5 g of HCPK. Surface-energy-controlled PUA solutions were synthesized using 3.0 g of urethan diacrylate oligomer, 1.0 g of HCPK, and 6.0 g of HEA (relatively hydrophilic), TFMA (relatively hydrophobic), or PFPE (relatively hydrophobic). The solutions were sonicated for 10 min at room temperature. Then, the mixtures were spread on a silicon wafer and rubbed after covering with a polycarbonate film. Finally, the prepared mediator was cured by exposure to ultraviolet (UV) light for 10 min.

2.3 | Device fabrication

The glass/indium tin oxide (ITO) substrate was cleaned using sonication equipment for 20 min with distilled water, acetone, and 2-propanol sequentially and then blown with nitrogen (N_2) gas to eliminate residual substances. Before spin-coating PEDOT:PSS onto the glass/ITO substrate, for hydrophilic surface modification, the prepared substrate was treated with UV-ozone for 10 min. PEDOT:PSS was formed by spin-coating at 5000 rpm for 40 s and thermally annealed at 140°C for 10 min. The PM6:BTP-4F-12 solution, in a weight ratio of 1.0:1.2 (at a concentration of 22 mg mL^{-1}), was added to o-xylene with 1-chloronaphthalene (0.5 vol%). PM6-4F-12 was spin-coated onto PEDOT:PSS-coated substrates or VF-laminated mediators. Subsequently, for VF lamination, PM6:BTP-4F-12 was VF-laminated from

the mediators to the PEDOT:PSS layer at 110°C on a hot plate and thermally treated at 150°C for 10 min. After that, PDINN (1.0 mg ml^{-1} in MeOH), as an electron transport layer with a thickness of approximately 10 nm, was spin-coated at 5000 rpm for 40 s. Finally, a Ag cathode with a thickness of 100 nm was thermally evaporated onto the prepared device using a shadow mask at 4.0×10^{-6} Torr using a thermal evaporator.

2.4 | Characterization

UV–visible spectroscopy (PerkinElmer Lambda 365) measurements were performed to investigate the light absorption of the PM6:BTP-4F-12. The photoluminescence (PL) spectra were investigated using a Hitachi F-7000 fluorescence spectrophotometer at an excitation wavelength of 600 nm. PV and photodetection performances were determined using a solar simulator (PEC-L01; Peccell Tech, Inc.) under AM 1.5 G 100 mW cm^{-2} (1-sun condition) calibrated with a silicon reference device. J–V characterizations were performed using an electrical measurement system (ZIVE SP1). The external quantum efficiency (EQE) spectra measurement was performed using a monochromator (MonoRa-500i; Dongwoo Optron Co., Ltd.) after power calibration (LS150; ABET Tech Inc.). Impedance spectroscopy of the devices was performed using a potentiostat (ZIVE SP1; Zivelab). Photo responses were obtained after amplifying 1000 times using a variable gain amplifier (DLPCA-200; Femto Messtechnik Gmbh). All electronic measurements were performed in a dark metal box (Faraday cage) for electron shielding. The thickness of the thin film and surface morphology of the thin films were determined by alpha-step and atomic force microscope (AFM) in noncontact mode (Park NX10), respectively. X-ray photoelectron spectroscopy (XPS) measurements were carried out using a K-Alpha+ spectrometer (Thermo Fisher Scientific).

3 | RESULTS AND DISCUSSION

Figure 1A illustrates the chemical structure of PM6 as a polymer donor and BTP-4F-12 as a nonfullerene acceptor. All the devices fabricated were consistent with normal structure configurations consisting of ITO/ PEDOT:PSS/PM6:BTP-4F-12/PDINN/Ag (Figure 1B). Furthermore, to realize reproducible VF lamination by transferring the hydrophobic PM6:BTP-4F-12, we introduced UV-curable PUA as the laminating mediator and controlled the adhesion property based on the work of adhesion (ω_a) values (Figure 1C).[22]

Specifically, the adhesion-controlled mediators were designed, considering the various surface energies from hydrophobic to hydrophilic, by introducing PUA-PFPE, PUA-2,2,2-trifluoroethyl methacrylate (TFMA) and PUA-2-hydroyxyethyl acrylate (HEA). The mediators were fabricated by the reaction between the polar functional chains of the reactive agent and UA oligomers and were adopted as the transfer mechanism for the lamination of PM6:BTP-4F-12 layers onto the PEDOT:PSS-coated substrate. The ω_a values were obtained by calculating the surface energies of various VF lamination mediators from the contact angle measurements (Figure S1 and Table S1). From the ω_a values, it is clear that when the mediator has low surface energy due to the addition of a reactive agent like PFPE or TFMA, it shows low adhesive properties, which induces a nonuniform surface on these mediators. Meanwhile, when the 2-HEA (hydrophilic reactive agent) was added to the PUA, it showed high surface energy, which shows improved adhesion behavior with hydrophobic PM6:BTP-4F-12 (Figure S2 and Table S2). Therefore, we adopted the PUA-HEA mediator for the reproducible VF lamination process and achieved successful fabrication using the UV-curing system as shown in Figure 1D.

Moreover, to implement well-formed thin films through the VF lamination process, the interfacial energies among the target material, mediator, and PEDOT:PSS surface were calculated by considering the surface energy of the PEDOT:PSS, following the Owen–Wendt method using Young's equation given below:

$$\gamma_{lv}(1 + \cos\theta) = 2\sqrt{\gamma_{sv}^d \gamma_{lv}^d} + 2\sqrt{\gamma_{sv}^p \gamma_{lv}^p}, \tag{1}$$

$$\gamma_{sl} = \gamma_{sv} + \gamma_{lv} - 2\sqrt{\gamma_{sv}^d \gamma_{lv}^d} - 2\sqrt{\gamma_{sv}^p \gamma_{lv}^p}, \tag{2}$$

where θ is the contact angle; γ_{lv}, γ_{lv}^d, and γ_{lv}^p represent the liquid surface free energy, the dispersive surface energy, and polar surface energy, respectively. By using Young's equation, the interfacial energies can be calculated among the PUA-HEA, PM6:BTP-4F-12, and PEDOT:PSS substrates. The interfacial energy between PM6:BTP-4F-12 and PUA-HEA was 4.14 mJ m^{-2} and that between PM6:BTP-4F-12 and PEDOT:PSS was 11.05 mJ m^{-2}. This result indicates that the interfacial energy between PM6:BTP-4F-12 and PEDOT:PSS is stronger than that between PM6:BTP-4F-12 and PUA-HEA so that PM6:BTP-4F-12 is successfully delaminated from the mediator and formed onto the PEDOT:PSS substrate.

In general, although the donor and the acceptor mixed properly, when spin-coating was performed, it induced an
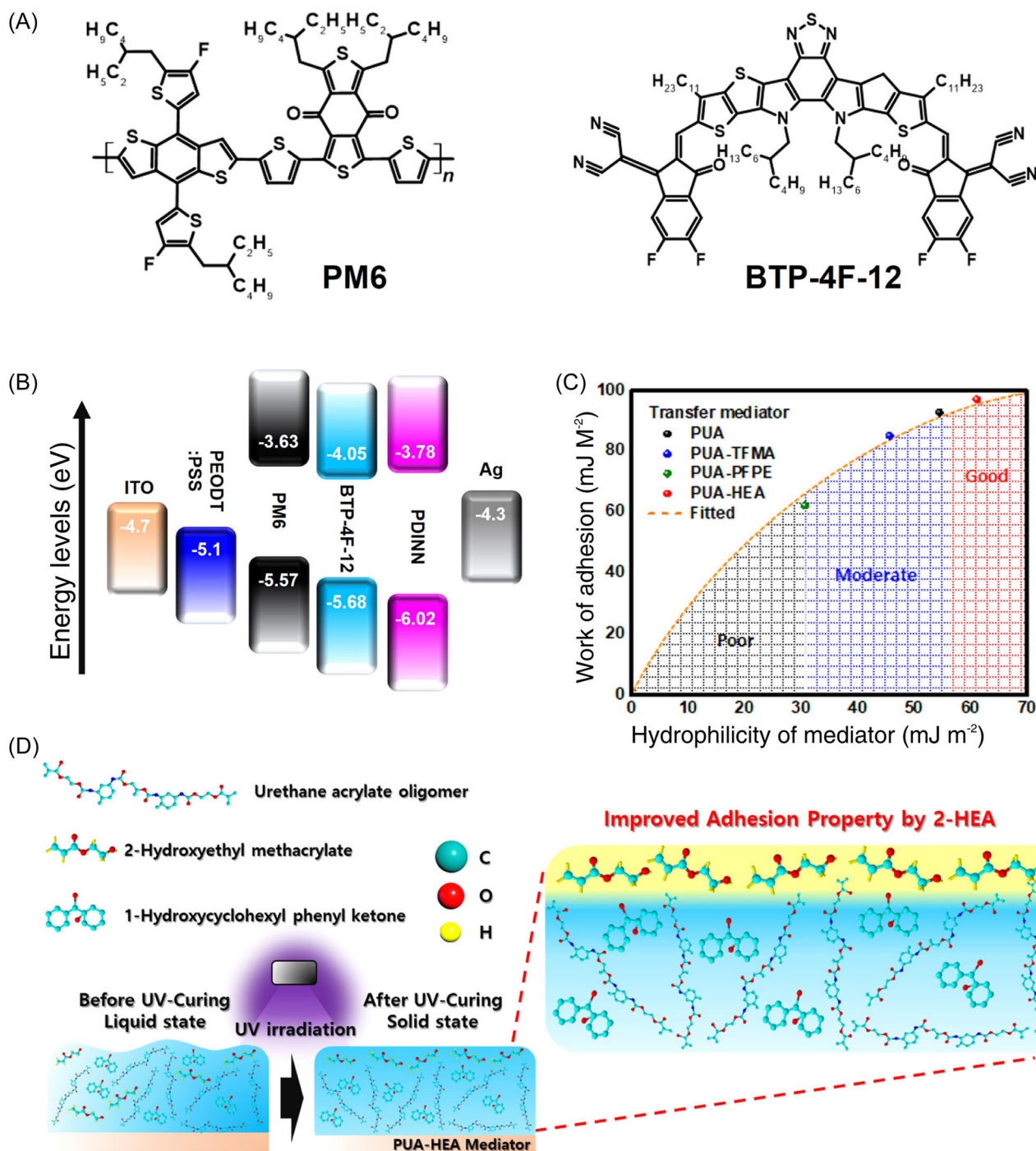
FIGURE 1 (A) Molecular structure of the PM6 donor and the BTP-4F-12 acceptor, (B) energy-level diagram of the device, (C) calculated adhesion property between the target (PM6:BTP-4F-12) and the transfer mediator, and (D) schematic of the adhesion-optimized polymer mediator by using 2-HEA reactive agent.

unexpected phase segregation owing to the difference in the surface energy of the materials, and small-molecular NFAs tend to move during the film formation.[23] Specifically, the donor component is mainly located at the surface of the active layer, while the acceptor component is located toward the bottom. Therefore, from observation of spin-coated PM6:BTP-4F-12, it is clear that the PM6 components dominantly occupy the surface, while the BTP-4F-12 components mainly occupy the bottom. This indicates that PM6 makes contact with PDINN as the electron transfer layer (ETL) and BTP-4F-12 makes contact with PEDOT:PSS as the hole transfer layer (HTL), inducing inefficient charge transport in the normal structure (Figure S3). Conversely, the VF lamination can

modify this by reversing the surface morphology that turned upside down during the process (Figure 2A). In previous studies, the thin-film transfer process was performed only on a single material or a solution-processed material with a specific thickness. However, as shown in Figure 2B, we successfully conducted the film-transfer lamination process on photoactive materials with thickness from very thin to thick based on the optimized adhesive property adopting HEA-PUA as the VF-laminating mediator and investigated thickness-dependent absorption properties (Figure S4).

To achieve the above-stated goal, we investigated the surface component of the PM6:BTP-4F-12 film with different processes using an XPS analysis. In particular, before observing the process-dependent PM6:BTP-4F-12 layer, we checked the surface component of the PM6 and BTP-4F-12-only layer. Figure 3A shows the survey spectra of pristine PM6 and BTP-4F-12, and we focused on the difference in their representative elements such as fluorine (F) and nitrogen (N).[24]

Based on the chemical structure of each material, it is clear that PM6 does not have any N element, but BTP-4F-12 does. For BTP-4F-12, we observed clear N 1s and F 1s peaks around the binding energies (BEs) of 400 and 680 eV, respectively, indicating that it contained N and more F components than PM6.

Based on this, the process-dependent PM6:BTP-4F-12 layer was also investigated, and in the VF-laminated PM6:BTP-4F-12 film, we observed higher N 1s and F 1s peaks than in the spin-coated devices, which is consistent with the result of pristine BTP-4F-12 as shown in Figure 3B. From the above results, it was confirmed again that the spin-coated PM6:BTP-4F-12 had PM6-rich components at the surface of the film and BTP-4F-12-rich components at the surface of VF-laminated PM6:BTP-4F-12.

To obtain more information, we performed fitting of the F 1s peak of PM6:BTP-4F-12 based on different coating processes. As shown in Figure 3C, both the PM6:BTP-4F-12 layer prepared by spin-coating and VF lamination showed a semi-ionic C–F bond and a covalent C–F bond. In particular, PM6:BTP-4F-12 with VF lamination shifted to a high BE for the semi-ionic (687.4 eV) and covalent (688.5 eV) bonds, indicating a strong binding force between C and F. Consequently, the higher the C–F bond intensity, as a result of high electronegativity of F, the better the internal charge transport ability.[25,26] From the fitted N 1s spectra (Figure 3D), C=N–C (around 399 eV), C=N (around 400 eV), and N–H (around 688 eV) bonds were found in PM6:BTP-4F-12 with both processes. From the N 1s spectra, narrower peaks that shifted to a higher BE were also observed in the VF-laminated PM6, similar to the F 1s spectra.[27–29] These XPS results provide convincing evidence that the VF lamination process can induce the phase-switching effect, based on the observation of the acceptor-rich component at the surface of the PM6:BTP-4F-12 film.

Specifically, we fabricated PV (Figure S5) and, subsequently, studied the photodetecting (PD) (Figure S6) applications using various thicknesses of PM6:BTP-4F-12 prepared by different processes. The detailed device performances are summarized in Tables S3 and S4. On comparing the above results, it was confirmed that 110 and 240 nm PM6:BTP-4F-12 showed optimized thickness for PV (Figure 4A, left) and PD applications (Figure 4A, right), respectively.

For the PV device based on PM6:BTP-4F-12 of 110 nm, prepared by VF lamination, we observed better performance (PCE of 15.97%), with an open circuit voltage (V_{OC}) of 0.838 V, a short-circuit current density (J_{SC}) of 26.97 mA cm^{-2}, and a fill factor (FF) of 0.71, than that prepared using the spin-coating process (PCE of 15.30%), as shown in
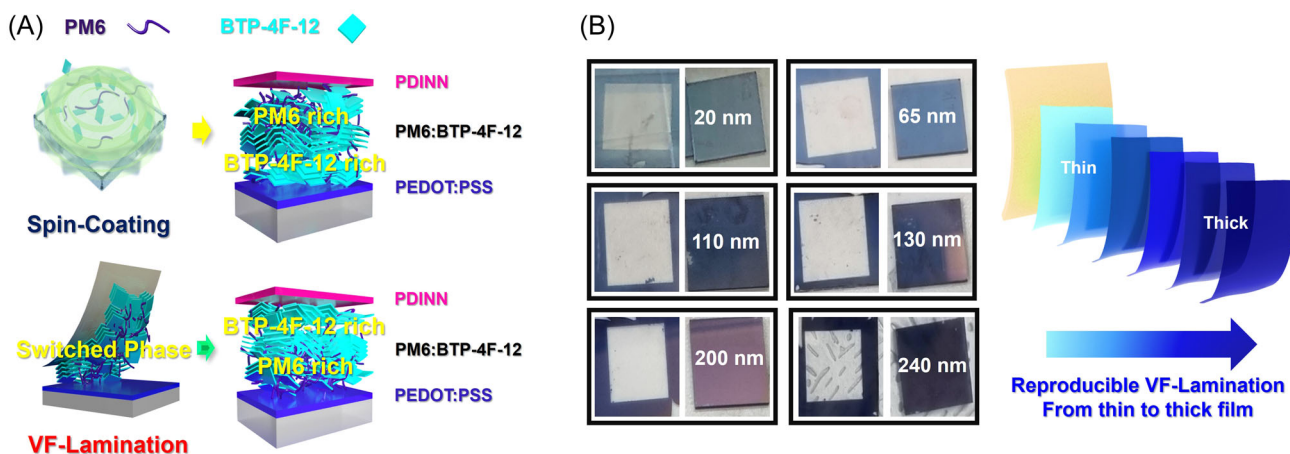

FIGURE 2 (A) Schematic of spin-coating and VF lamination process for PM6:BTP-4F-12 by the adhesion-optimized PUA-HEA mediator. (B) Photographs of the VF-laminated PM6:BTP-4F-12 (from 20 to 240 nm).
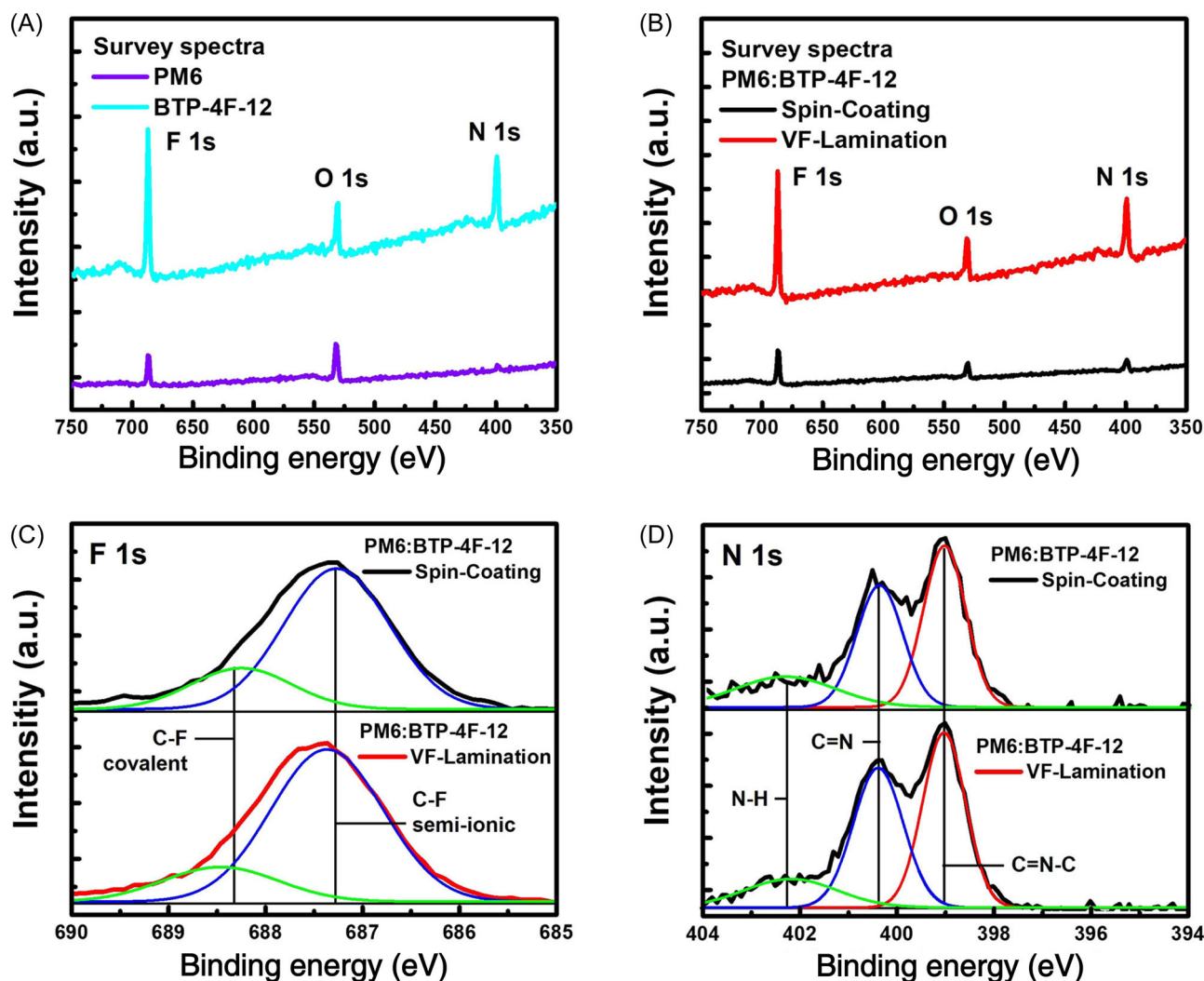
FIGURE 3 XPS survey spectra of the (A) pristine PM6 and BTP-4F-12 layer and (B) PM6:BTP-4F-12 layer prepared by different processes. Fitted (C) F 1s spectra and (D) N 1s spectra for the PM6:BTP-4F-12 layer with different processes.

Figure 4B. The detailed PV parameters and reproducibility are presented in Table 1 and Figure S7, respectively. The current density under 840-nm light illumination showed improvements, which is in agreement with the EQE trend (Figure 4C) as shown in Figure 4D. These thickness- and process-dependent results showed a similar trend as the PL intensity, which consisted of an ITO/PEDOT:PSS/active layer/PDINN structure (Figure S8).

For the PD application, the dark current density (J_{dark}) reduction is key to improving the performances, and the VF-laminated device showed a slightly lower J_{dark} (5.86×10^{-10} A cm^{-2}) than the spin-coated device (1.02×10^{-9} A cm^{-2}) under the 0 V condition, which indicates a higher shunt resistance, as shown in Figure 4E. To clearly compare the photocurrent, photo-responsivity (R), which converts incident light into photocurrent output, is calculated using the following

Equation (3), where J_{photo} is the photocurrent density, L_{light} indicates the incident light density, and λ is the wavelength of the incident light.

$$R = \frac{J_{photo}}{L_{light}} = \frac{EQE}{100\%} \times \frac{\lambda}{1240}. \quad (3)$$

Figure 4F shows that the VF-laminated device shows a higher value of 0.50 A W^{-1} than the spin-coated device (0.48 A W^{-1}), which is similar to the EQE spectra. As shown in Figure 4G, D^* has been widely used to estimate the photosensitivity in the PD application. Specifically, dark current (I_{dark}) is often considered the most important factor that influences the noise current.[30,31] Accordingly, the detectivity (D^*)^n value of the devices is estimated by simplifying the noise-limited D^* based on the following equation:
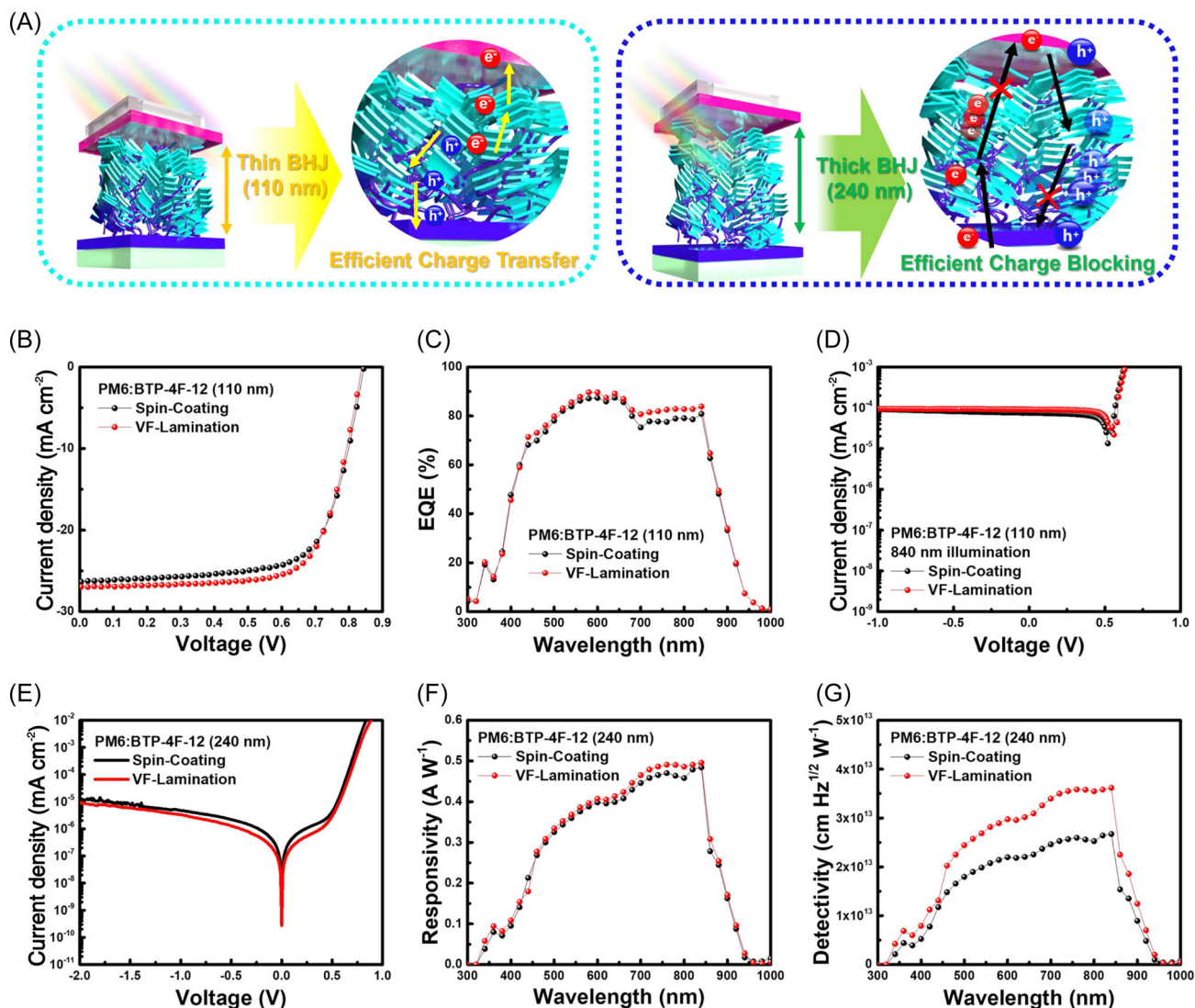
FIGURE 4 (A) Optimized PM6:BTP-4F-12 thickness condition for photovoltaic (110 nm, left) and photodetecting (240 nm, right) applications. Photovoltaic performances: (B) J–V characteristics under AM 1.5 G irradiation at 100 mW cm^{-2}. (C) EQE spectra and (D) photocurrent under 840 nm light illumination. Photodetecting performances: (E) J–V characteristics under dark conditions, (F) photoresponsivity, and (G) detectivity under 0 V bias obtained from J_{dark}.

TABLE 1 Photovoltaic performances of the PM6:BTP-4F-12 (110 nm)-based devices prepared by different processes.

PM6:BTP-4F-12 (110 nm)	V_{OC} (V)	J_{SC} (mA cm^{-2})	J_{SC}^{EQE} (mA cm^{-2})	FF	PCE (%)
Spin-coating	0.844 (0.834 ± 0.01)	26.33 (26.11 ± 0.64)	25.31 (25.64 ± 0.77)	0.69 (0.69 ± 0.03)	15.30 (14.95 ± 0.48)
VF lamination	0.838 (0.838 ± 0.01)	26.97 (26.60 ± 0.46)	26.12 (25.74 ± 0.47)	0.71 (0.70 ± 0.01)	15.97 (15.58 ± 0.21)

Note: The average parameters were calculated from 10 devices, with an area of 0.15 cm^2. Values outside the parentheses denote the best device results.

Abbreviations: BTP-4F-12, 2,2′-((2Z,2′Z)-((12,13-bis(2-butyloctyl)-3,9-diundecyl-12,13-dihydro-[1,2,5]thiadiazolo[3,4-e]thieno[2′′,3′′:4′,5′]thieno[2′,3′:4,5] pyrrolo[3,2-g]thieno[2′,3′:4,5]thieno[3,2-b]indole-2,10-diyl)bis(methanylylidene))bis(5,6-difluoro-3-oxo-2,3-dihydro-1H-indene-2,1-diylidene))dimalononitrile; EQE, external quantum efficiency; PCE, power conversion efficiency; PM6, poly[(2,6-(4,8-bis(5-(2-ethylhexyl-3-fluoro)thiophen-2-yl)-benzo[1,2-b:4,5-b′] dithiophene))-alt-(5,5-(1′,3′-di-2-thienyl-5′,7′-bis(2-ethylhexyl)benzo[1′,2′-c:4′,5′-c′]dithiophene-4,8-dione)]; VF, vacuum-free.

$$D^* = \frac{R(\lambda)\sqrt{AB}}{i_{noise}} = \frac{R(\lambda)\sqrt{A}}{\sqrt{2qI_{dark}}} = \frac{R(\lambda)}{\sqrt{2qJ_{dark}}}, \quad (4)$$

where the $R(\lambda)$, A, and B indicate the responsivity at a specific wavelength, area, and J_{dark} of the devices,

respectively. In addition, i_{noise} and I_{dark} in the above equation indicate the noise current and dark current, respectively. The calculated D^* value, considering the J_{dark} with the VF-laminated devices, was higher (3.61×10^{13} cm Hz$^{1/2}$ W^{-1}) than that of the spin-coated devices due to not

only the charge-blocking property against external injection but also suppression of the leakage current. The detailed performances are summarized in Table 2.

To observe the difference in the surface morphologies of thin (110 nm) and thick (240 nm) PM6:BTP-4F-12 with different processes, AFM analysis was performed. More precisely, from the phase images, it is clear that in PM6:BTP-4F-12 of 110 nm with the spin-coating process, the donor components (black) are dominantly present at the surface (Figure 5A) and the acceptor components (white) mainly exist at the surface in the VF-laminated film (Figure 5B). This phenomenon is also observed in the thick

TABLE 2 Photodetecting performances of the PM6:BTP-4F-12 (240 nm)-based devices prepared by different processes.

PM6:BTP-4F-12 (240 nm)	J_{dark} (A cm^{-2})	Responsivity (A W^{-1})	Detectivity (cm Hz$^{1/2}$ W^{-1})
Spin-coating	1.02×10^{-9}	0.48	2.67×10^{13}
VF lamination	5.86×10^{-10}	0.50	3.61×10^{13}

Abbreviations: BTP-4F-12, 2,2′-((2Z,2′Z)-((12,13-bis(2-butyloctyl)-3,9-diundecyl-12,13-dihydro-[1,2,5]thiadiazolo[3,4-e]thieno[2′′,3′′:4′,5′]thieno[2′,3′:4,5]pyrrolo[3,2-g]thieno[2′,3′:4,5]thieno[3,2-b]indole-2,10-diyl)bis(methanylylidene))bis(5,6-difluoro-3-oxo-2,3-dihydro-1H-indene-2,1-diylidene))dimalononitrile; PM6, poly[(2,6-(4,8-bis(5-(2-ethylhexyl-3-fluoro)thiophen-2-yl)-benzo[1,2-b:4,5-b′]dithiophene))-alt-(5,5-(1′,3′-di-2-thienyl-5′,7′-bis(2-ethylhexyl)benzo[1′,2′-c:4′,5′-c′]dithiophene-4,8-dione)]; VF, vacuum-free.

(240 nm) film, as shown in Figure 5C,D. As the thickness of PM6:BTP-4F-12 increased, this difference obviously increased between spin-coating and VF lamination (Figures S9 and S10). These results are consistent with the above surface component analyses.[32,33]

Spin-coated PM6:BTP-4F-12 showed an R_q value of 0.956 nm (Figure 5E), and the VF-laminated device showed a root mean square surface roughness (R_q) value of 0.927 nm, indicating smoother surface morphology (Figure 5F). In addition, it is a well-known fact that a sharp surface morphology can contribute to the improvement of charge transfer ability, and our result is in agreement with the improved current density in the VF-laminated PV device. However, in the case of the thick (240 nm) film, the spin-coated device showed an increased R_q value of 1.544 nm (Figure 5G) and the VF-laminated device showed a much higher R_q value of 3.088 nm (Figure 5H). This originated from the strong phase separation, and the thick film tends to show stronger phase separation than the thin film.[34]

In particular, VF-laminated thick PM6:BTP-4F-12 showed a twofold higher roughness value than the spin-coated owing to the crystallinity of BTP-4F-12, dominantly present at the surface due to the morphology inversion effect.

To observe the internal charge transport and resistance of the PV device based on PM6:BTP-4F-12 of 110 nm prepared by spin-coating and VF lamination, we performed
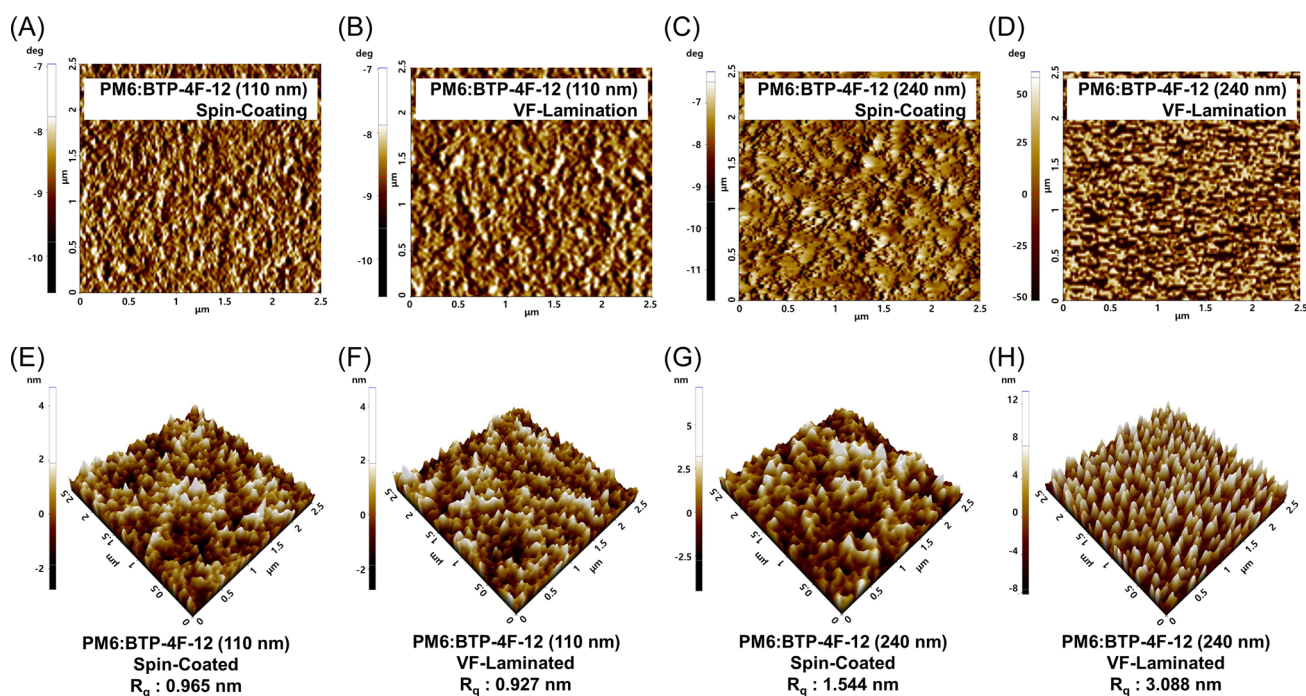

FIGURE 5 (A–D) AFM phase images and (E–H) three-dimensional height images of PM6:BTP-4F-12 (with respect to thickness) prepared by different processes.

optical and physical analyses. Precisely, the photocurrent density (J_{photo}) characterization of the PV applications was evaluated based on exciton generation behaviors. In the analysis, plots of J_{photo} versus internal voltage (V_{int}) were constructed using the formula $V_{int} = V_0 - V_{appl}$, where V_0 is the zero-voltage position of J_{photo} and V_{appl} is the applied voltage. Additionally, J_{photo} is calculated using the equation $J_{ph} = J_{light} - J_{dark}$, where J_{light} and J_{dark} indicate the characterized current densities under light illumination (1-sun) and dark conditions, respectively.[35] Based on the calculated $J_{photo} - V_{int}$ plot, the maximum exciton generation rate (G_{max}) values of the devices were calculated based on the following equation:

$$J_{sat} = q \times L \times G_{max}, \qquad (5)$$

where J_{sat}, q, and L indicate the saturated photocurrent density, electronic charge, and thickness of the active layer, respectively. As shown in Figure 6A, the device with VF lamination showed a slightly higher G_{max} value of $1.53 \times 10^{28}\,m^{-3}\,s^{-1}$ than the spin-coated device ($1.53 \times 10^{28}\,m^{-3}\,s^{-1}$).

Considering the G_{max} values, the PL intensity was determined for 110 nm PM6:BTP-4F-12 to observe the charge transfer properties through HTL and ETL (Figure 6B). Additionally, VF-laminated PM6:BTP-4F-12 demonstrated not only superior exciton generation properties but also lower PL intensity, indicating a favorable charge transfer mechanism compared to the spin-coated device because of the donor and acceptor interfaces with HTL and ETL, respectively.

Light on/off response speed measurements for the devices based on different processes with a light-emitting diode (LED) (light source of 454 nm) were performed, as shown in Figure 6C,D, respectively. Precisely, the response time period can be defined as the time required for the photocurrent values to rise (fall) from 10% (90%) to 90% (10%).[36] When the LED was on and off, the VF-laminated devices showed a faster response time, with a rise time (τ_{rise}) of 10.2 μs and a turned-off fall time (τ_{fall}) of 9.76 μs, compared with the spin-coated device. The detailed information is summarized in Table S5.

To determine the internal device resistance, impedance spectroscopy analyses were conducted for the PV applications, and these were performed for the internal voltage V_{OC} and 0 V state under 1-sun illumination. In the case of the internal voltage at V_{OC}, the light-induced voltage is confirmed, and the photogenerated charge carriers from the photoactive material are recombined before collecting at the electrode.[37] Accordingly, a semicircle scale at the V_{OC} is used to classify the photogenerated charge transport resistance (R_{CT}). The device with VF lamination (8.82 Ω) has slightly smaller scales than the spin-coated device,

indicating a lower R_{CT}, as shown in Figure 6E. Conversely, for the 0 V condition, the semicircle shows the charge recombination resistance (R_{REC}), and the larger semicircle indicates a favorable charge recombination suppression property. As shown in Figure 6F, the device with the VF lamination process yields better charge recombination property, with an R_{REC} of 2470 Ω based on a larger semicircle scale, than the spin-coated device. The detailed equivalent circuit and internal resistances are summarized in Figure S11 and Table S6, respectively. From the impedance analyses, the optimized ternary device was confirmed to have excellent charge transport and recombination characteristics under light illumination, and its excellent photoelectric conversion ability was also confirmed.

In terms of PD application, we performed space charge limited current (SCLC) analyses to confirm the charge mobility and trap density for the devices with PM6:BTP-4F-12 (thickness of 240 nm) based on different processes. For the calculated hole mobility from the hole-only devices (ITO/PEDOT:PSS/active layer/MoO$_x$/Ag), the spin-coated devices showed $1.97 \times 10^{-4}\,cm^2\,v^{-1}\,s^{-1}$ and VF-laminated devices showed a better result of $1.97 \times 10^{-4}\,cm^2\,v^{-1}\,s^{-1}$ (Figure 7A). Electron mobility was also calculated for electron-only devices (ITO/ZnO/active layer/PDINN/Ag), and the VF-laminated devices showed electron mobility of $3.90 \times 10^{-4}\,cm^2\,v^{-1}\,s^{-1}$ compared to the spin-coated devices ($2.72 \times 10^{-4}\,cm^2\,v^{-1}\,s^{-1}$) (Figure 7B). The detailed information on the charge mobility values is summarized in Table S7.

Meanwhile, trap densities are one of the criteria to investigate charge transport and recombination systems. Specifically, when the applied voltage is lower than that at the inflection point, the current linearly increases with the applied voltage, showing an Ohmic response. As the voltage exceeds the first inflection point, the current shows a steep nonlinear increase (slope > 3), indicating that all trap sites are filled by the injected charge carriers. Further, the applied voltage at the inflection point is represented as the trap-filled limit voltage (V_{TFL}), which is used to determine the trap state density. The trap density is calculated as given in the following equation:

$$V_{TFL} = \frac{eN_t d^2}{2\varepsilon_r \varepsilon_0}, \qquad (6)$$

where e indicates the elementary charge, d is the thickness of the active layer, and ε is the relative dielectric constant of the active material. For the hole-only devices, the trap density is represented by $N_{t,h}$, and for the electron-only devices, it is represented by $N_{t,e}$.[38] Accordingly, $N_{t,h}$ for the device prepared by VF lamination showed a slightly lower trap density of $1.09 \times 10^{15}\,\#\,cm^{-3}$ based on a low V_{TFL} (0.19 V). In addition, $N_{t,e}$ of the VF-laminated device was also calculated
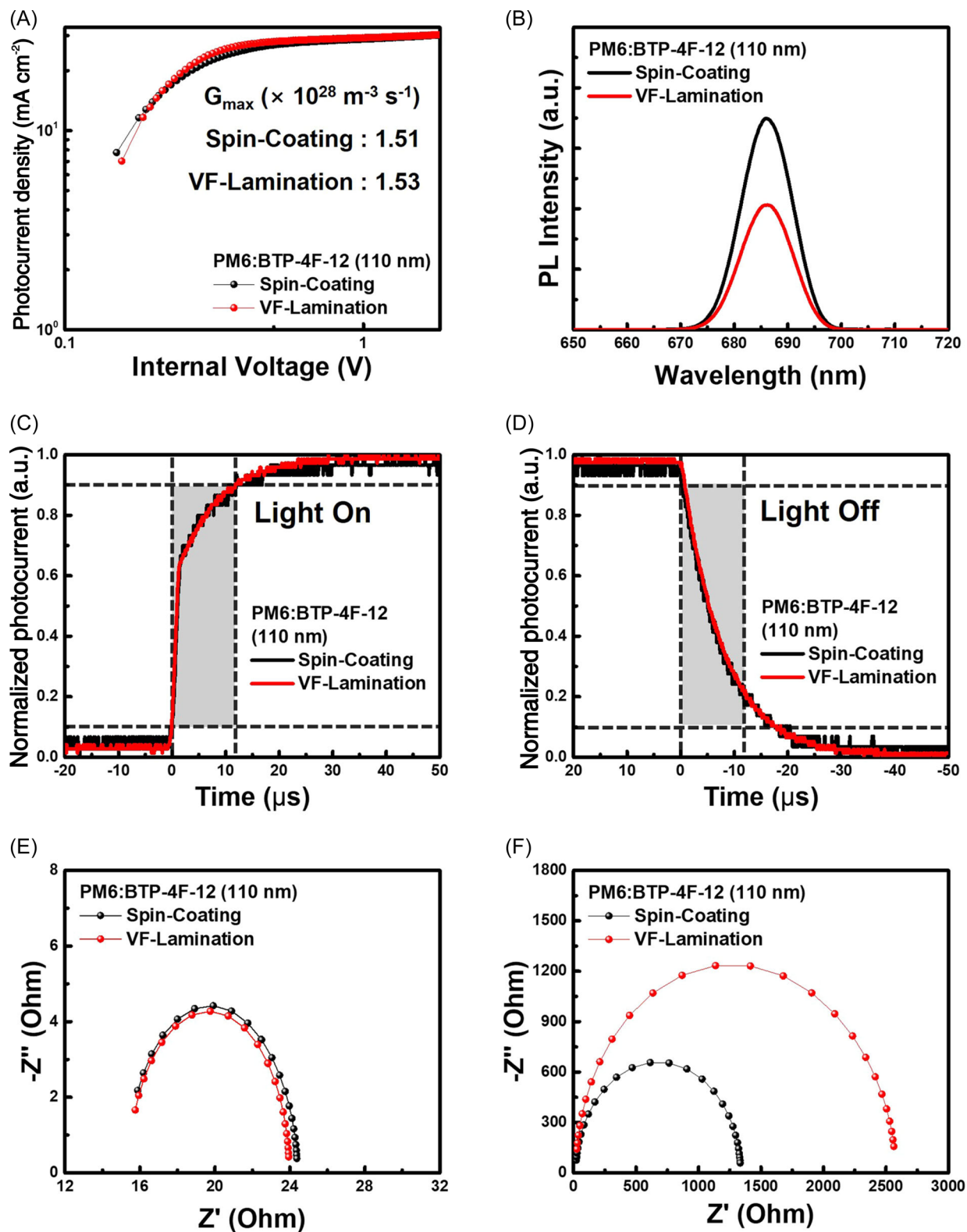
FIGURE 6 Additional analyses for the PV devices (PM6:BTP-4F-12, 110 nm) prepared by different processes. (A) Photocurrent density (J_{photo}) versus internal voltage (V_{int}) characterization. (B) PL spectra. Light source (C) on and (D) off photoresponse speed measurement. Impedance spectroscopy (under AM 1.5 G illumination) at sample biases of (E) V_{OC} and (F) 0 V condition.
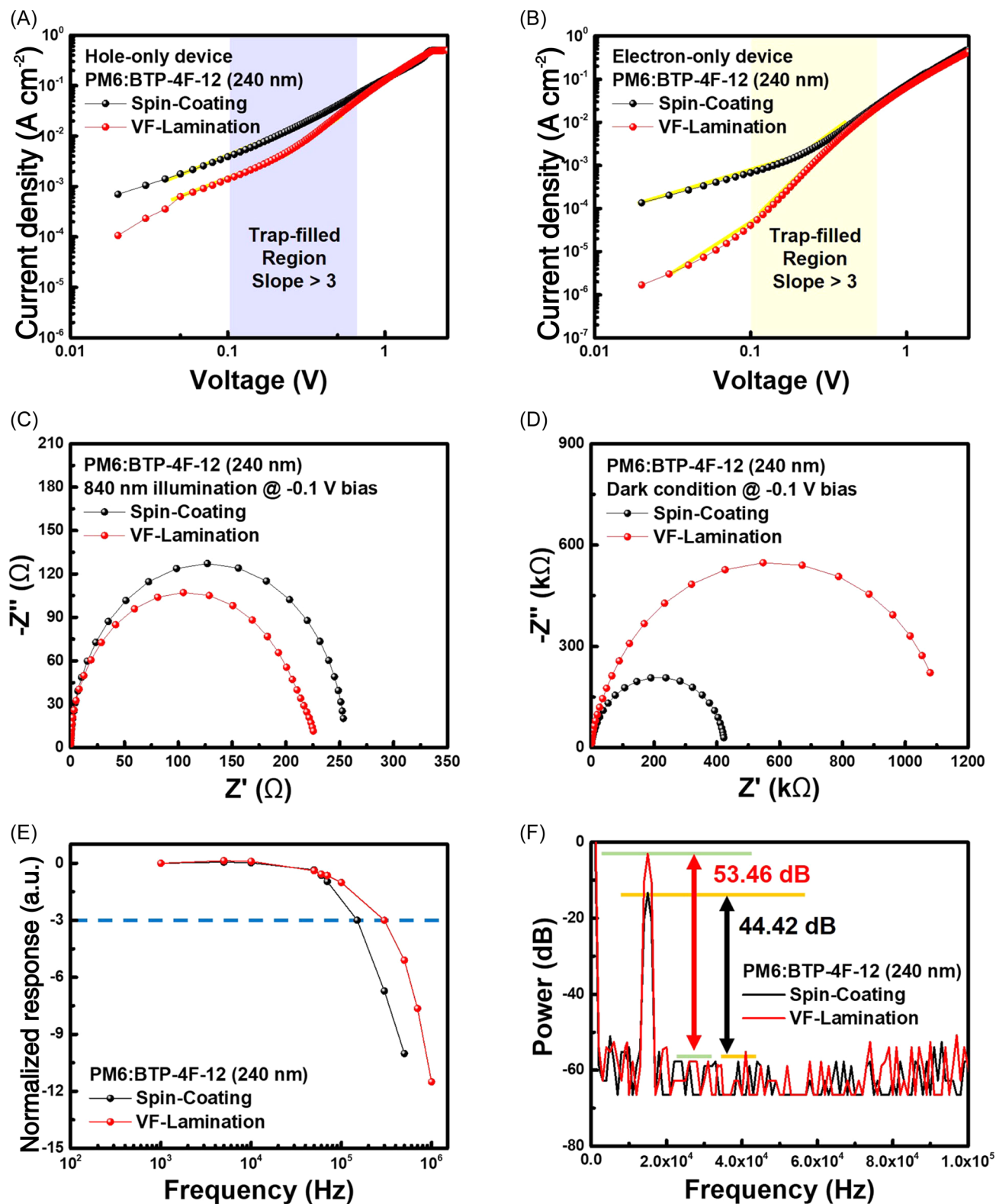
FIGURE 7 Additional analyses for the PD devices (PM6:BTP-4F-12, 240 nm) prepared by different processes. SCLC plots of the (A) hole-only and (B) electron-only devices. Impedance spectroscopy (C) under illumination at 840 nm light and (D) under dark conditions of −0.1 V bias. (E) Frequency-dependent responses and (F) signal-to-noise ratios.

to be 8.07×10^{14} # cm^{-3}, indicating a lower trap density on account of a V_{TFL} of 0.14 V. The detailed information of the trap density values is summarized in Table S8.

Furthermore, impedance spectroscopy measurements were conducted under light illumination (840 nm) and dark conditions. Specifically, the series resistance values were calculated from the impedance responses under illumination by using an 800-nm LED light. More precisely, the PM6:BTP-4F-12-based device with VF lamination showed a series resistance of 217.1 Ω, which is lower than that of the spin-coated device (260.1 Ω) (Figure 7C). Under dark conditions, the VF-laminated PM6:BTP-4F-12-based device showed a shunt resistance of 1079.4×10^3 Ω, whereas the spin-coating-based device showed a shunt resistance of 403.8×10^3 Ω (Figure 7D). Based on the above results, it is clear that the VF-laminated device shows favorable charge transport due to its low series and high shunt resistance resistances.[39,40]

To evaluate the optical responses in depth, we used a −3-dB cutoff frequency (f_{-3dB}) under a light pulse for the PD devices prepared by different processes. Specifically, the f_{-3dB} is the evaluation index of the PDs when the signal decays by 50% relative to the initial signal.[41] The f_{-3dB} of the device based on VF lamination showed a higher value (over 300 kHz) than the spin-coated device under 150 kHz (Figure 7E). The signal-to-noise ratio (SNR) obtained from the fast Fourier transform test is another index of PD performance.[42] The VF-laminated device showed a higher SNR value of 53.46 dB compared to the spin-coated device (44.42 dB). This result indicates that the VF-laminated device showed a reduced noise current value due to the dark current suppression caused by the surface morphology inversion effect (Figure 7F).

Figure 8A,B illustrates the internal photo-generated charge transport and external charge injection mechanism of the VF-laminated PM6:BTP-4F-12 layer-based PV
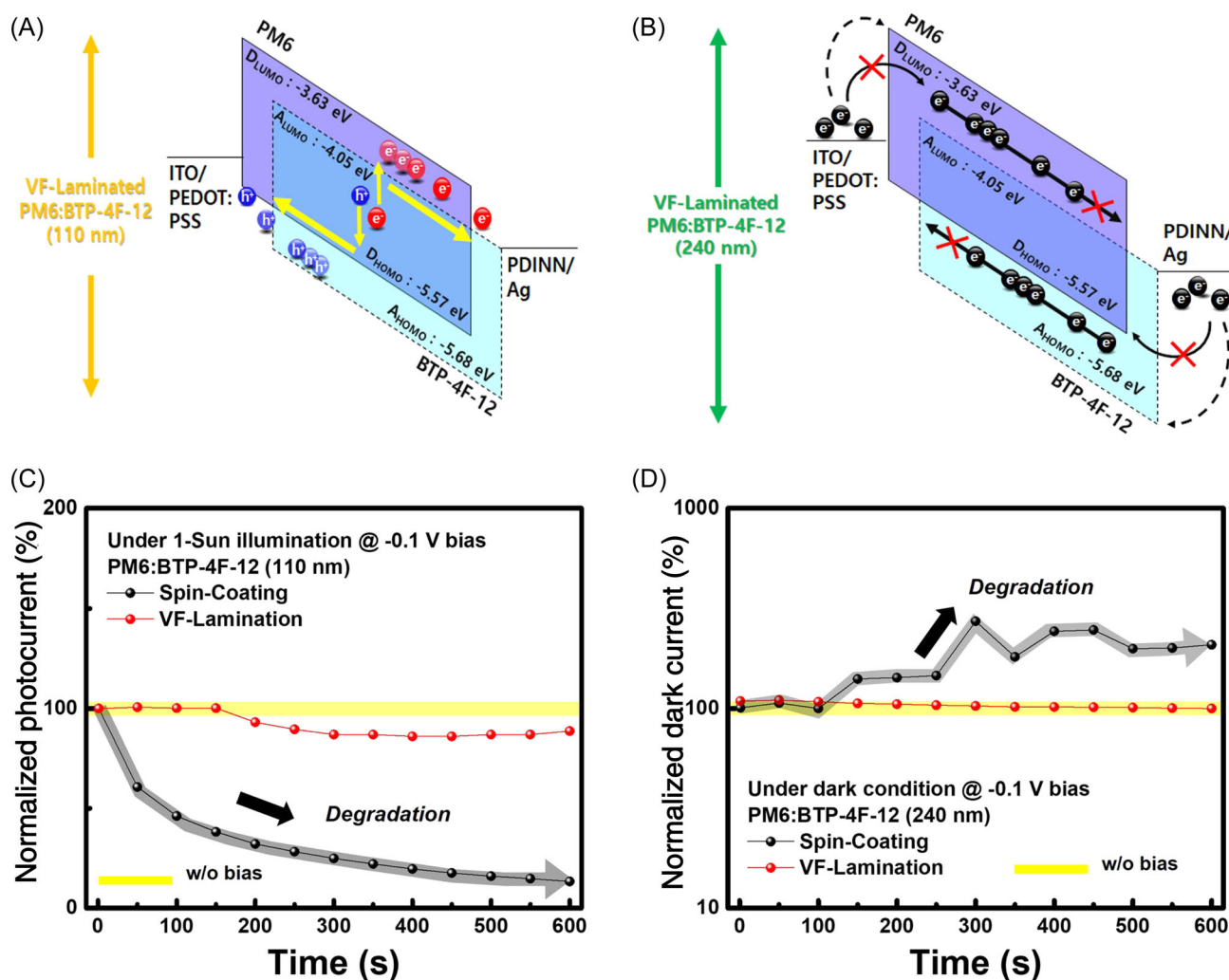

FIGURE 8 Schematic of (A) charge transport and (B) injected charge-blocking mechanism of VF-laminated PM6:BTP-4F-12. Normalized time-dependent electrical stability (applied −0.1 V bias) under (C) 1-sun illumination (PM6:BTP-4F-12, 110 nm) and (D) dark conditions (PM6:BTP-4F-12, 240 nm) for the devices prepared by different processes.

(110 nm) and PD (240 nm) devices, respectively. For the PV devices (Figure 8C), the normalized photocurrent is measured during 600 s, under 1-sun illumination and an applied bias of −0.1 V. The spin-coated devices showed a markedly reduced photocurrent after 50 s due to the externally applied bias, whereas the VF-laminated device showed a slightly reduced photocurrent after 150 s compared to the initial state. Furthermore, for the PD device (Figure 8D), dark current was also examined in the same manner. The spin-coated device showed poor stability after 100 s, and its dark current increased approximately twice after 200 s. Meanwhile, the VF-laminated device showed a stable operation at 600 s without any abnormal behavior. These efficient PV and PD performances of the VF-laminated device originated from the switched surface phase of PM6:BTP-4F-12. When PM6 is in contact with PEDOT:PSS and BTP-4F-12 is interfaced with PDINN via VF lamination, the charge transport ability of the photo-generated charge carriers improves. In addition, the low and stable dark current behavior of the VF-laminated device is due to the fact that the externally injected charge through each electrode has to encounter challenges to pass over the high lowest unoccupied molecular orbital (or highest occupied molecular orbital) level of PM6 (or BTP-4F-12).[43]

4 | CONCLUSION

In summary, we developed a reproducible VF lamination process (thin-film coating technique) by optimizing the surface adhesion of a polymer-based thin-film transfer mediator by the introduction of a polar functional reactive agent. Besides, we introduced this novel process in a bulk heterojunction system consisting of a polymer donor (PM6) and a nonfullerene acceptor (BTP-4F-12), and then successfully demonstrated the effectiveness of the process in thin (20 nm) and thick (240 nm) films. Specifically, the reversal phenomenon of surface morphology was identified through a detailed analysis of the surface component and its chemical bonding. Interestingly, the VF lamination process contributes to efficient charge transport and injected charge-blocking abilities, which leads to improved photo and reduced dark currents. Consequently, the VF-laminated PM6:BTP-4F-12-based devices showed improved PV (PCE of 15.97%) and PD (D^* of 3.61×10^{13} cm Hz$^{1/2}$ W^{-1}) performances. Additionally, the device prepared using VF lamination showed improved internal resistance as well as photo-response property, as confirmed by optical, electrical, and morphological analyses. Therefore, this innovative thin-film formation process is a promising strategy for solution-processable conjugated material-based devices as well as high-performance PV and PD devices.

CONFLICT OF INTEREST STATEMENT

The authors declare that there are no conflicts of interests.

ORCID

Dong Hwan Wang https://orcid.org/0000-0003-3736-3721

REFERENCES

1. Granström M, Petritsch K, Arias AC, Lux A, Andersson MR, Friend RH. Laminated fabrication of polymeric photovoltaic diodes. *Nature.* 1998;395(6699):257-260.
2. Chow PCY, Someya T. Organic photodetectors for next-generation wearable electronics. *Adv Mater.* 2020;32(15):1902045.
3. Wang C, Zhang X, Hu W. Organic photodiodes and photo-transistors toward infrared detection: materials, devices, and applications. *Chem Soc Rev.* 2020;49(3):653-670.
4. Zhou W, Shang Y, García de Arquer FP, et al. Solution-processed upconversion photodetectors based on quantum dots. *Nat Electron.* 2020;3(5):251-258.
5. Dou L, Liu Y, Hong Z, Li G, Yang Y. Low-bandgap near-IR conjugated polymers/molecules for organic electronics. *Chem Rev.* 2015;115(23):12633-12665.
6. Shang H, Fan H, Liu Y, Hu W, Li Y, Zhan X. A solution-processable star-shaped molecule for high-performance organic solar cells. *Adv Mater.* 2011;23(13):1554-1557.
7. Zhu L, Zhang M, Xu J, et al. Single-junction organic solar cells with over 19% efficiency enabled by a refined double-fibril network morphology. *Nat Mater.* 2022;21(6):656-663.
8. Wei Y, Chen Z, Lu G, et al. Binary organic solar cells breaking 19% via manipulating the vertical component distribution. *Adv Mater.* 2022;34(33):2204718.
9. Xing S, Nikolis VC, Kublitski J, et al. Miniaturized VIS-NIR spectrometers based on narrowband and tunable transmission cavity organic photodetectors with ultrahigh specific detectivity above 10^{14} jones. *Adv Mater.* 2021;33(44):2102967.
10. Zhang B, Trinh MT, Fowler B, et al. Rigid, conjugated macrocycles for high performance organic photodetectors. *J Am Chem Soc.* 2016;138(50):16426-16431.
11. Zhao H, Lin B, Xue J, et al. Kinetics manipulation enables high-performance thick ternary organic solar cells via R2R-compatible slot-die coating. *Adv Mater.* 2022;34(7):2105114.
12. Van Franeker JJ, Turbiez M, Li W, Wienk MM, Janssen RAJ. A real-time study of the benefits of co-solvents in polymer solar cell processing. *Nat Commun.* 2015;6:6229.

13. Wang J, Zheng Z, Zu Y, et al. A tandem organic photovoltaic cell with 19.6% efficiency enabled by light distribution control. *Adv Mater*. 2021;33(39):2102787.

14. Dong X, Jiang Y, Sun L, et al. Large-area organic solar modules with efficiency over 14%. *Adv Funct Mater*. 2022; 32(15):2110209.

15. Wei Y, Chen H, Liu T, et al. Self-powered organic photodetectors with high detectivity for near infrared light detection enabled by dark current reduction. *Adv Funct Mater*. 2021;31(52):2106326.

16. Chen M, Liu D, Li W, et al. Influences of non-fullerene acceptor fluorination on three-dimensional morphology and photovoltaic properties of organic solar cells. *ACS Appl Mater Interfaces*. 2019;11(29):26194-26203.

17. Ye L, Xiong Y, Chen Z, et al. Sequential deposition of organic films with eco-compatible solvents improves performance and enables over 12%-efficiency nonfullerene solar cells. *Adv Mater*. 2019;31(17):1808153.

18. Carlson A, Bowen AM, Huang Y, Nuzzo RG, Rogers JA. Transfer printing techniques for materials assembly and micro/nanodevice fabrication. *Adv Mater*. 2012;24(39):5284-5318.

19. Chaturvedi N, Gasparini N, Corzo D, et al. All slot-die coated non-fullerene organic solar cells with PCE 11%. *Adv Funct Mater*. 2021;31(14):2009996.

20. Ji G, Zhao W, Wei J, et al. 12.88% Efficiency in doctor-blade coated organic solar cells through optimizing the surface morphology of a ZnO cathode buffer layer. *J Mater Chem A*. 2019;7(1):212-220.

21. Kim MS, Jang W, Nguyen TQ, Wang DH. Morphology inversion of a non-fullerene acceptor via adhesion controlled decal-coating for efficient conversion and detection in organic electronics. *Adv Funct Mater*. 2021;31(38):2103705.

22. Wu S. *Polymer Interface and Adhesion*. Dekker; 1982.

23. He X, Chan CCS, Kim J, et al. 1-Chloronaphthalene-induced donor/acceptor vertical distribution and carrier dynamics changes in nonfullerene organic solar cells and the governed mechanism. *Small Methods*. 2022;6(3):2101475.

24. Watts JF, Wolstenholme J. *An Introduction to Surface Analysis by XPS and AES*. John Wiley and Sons; 2003.

25. Kandambeth S, Dey K, Banerjee R. Covalent organic frameworks: chemistry beyond the structure. *J Am Chem Soc*. 2019;141(5):1807-1822.

26. Liu X, Li X, Li Y, et al. Regulating the bonding nature and location of C–F bonds in fluorinated graphene by doping nitrogen atoms. *Ind Eng Chem Res*. 2021;60(2):875-884.

27. Gao Y, Hou F, Hu S, et al. Graphene quantum-dot-modified hexagonal tubular carbon nitride for visible-light photocatalytic hydrogen evolution. *ChemCatChem*. 2018;10(6):1330-1335.

28. Majumdar A, Das SC, Shripathi T, Hippler R. Chemical synthesis and surface morphology of amorphous hydrogenated carbon nitride film deposited by N_2/CH_4 dielectric barrier discharge plasma. *Compos Interfaces*. 2012;19(3-4):161-170.

29. Huang Z, Chen H, Zhao L, et al. In suit inducing electron-donating and electron-withdrawing groups in carbon nitride by one-step NH_4Cl-assisted route: a strategy for high solar hydrogen production efficiency. *Environ Int*. 2019;126:289-297.

30. Yang K, Zhao Z, Liu M, et al. Highly sensitive broadband photomultiplication type all-polymer photodetectors and their applications in optical pulse counting. *J Mater Chem C*. 2022;10(30):10888-10894.

31. Gong X, Tong M, Xia Y, et al. High-detectivity polymer photodetectors with spectral response from 300 nm to 1450 nm. *Science*. 2009;325(5948):1665-1667.

32. Kim MS, Luo D, Jang W, et al. High-sensitivity organic photodetector based on surface-concentrated nonfused ring electron acceptor. *Adv Opt Mater*. 2023;11(5):2202525.

33. Nilsson S, Bernasik A, Budkowski A, Moons E. Morphology and phase segregation of spin-casted films of polyfluorene/PCBM blends. *Macromolecules*. 2007;40(23):8291-8301.

34. Lee S, Park KH, Lee JH, et al. Achieving thickness-insensitive morphology of the photoactive layer for printable organic photovoltaic cells via side chain engineering in nonfullerene acceptors. *Adv Energy Mater*. 2019;9(14):1900044.

35. Jung JW, Jo JW, Chueh CC, et al. Fluoro-substituted n-type conjugated polymers for additive-free all-polymer bulk hetero-junction solar cells with high power conversion efficiency of 6.71%. *Adv Mater*. 2015;27(21):3310-3317.

36. Liu M, Fan Q, Wang J, et al. Double-layered strategy for broadband photomultiplication-type organic photodetectors and achieving narrowband response in violet, red, and near-infrared light. *ACS Appl Mater Interfaces*. 2022;14(40):45636-45643.

37. Xu L, Lee YJ, Hsu JWP. Charge collection in bulk heterojunction organic photovoltaic devices: an impedance spectroscopy study. *Appl Phys Lett*. 2014;105(12):123904.

38. Blakesley JC, Neher D. Relationship between energetic disorder and open-circuit voltage in bulk heterojunction organic solar cells. *Phys Rev B*. 2011;84(7):075210.

39. Lan Z, Lei Y, Chan WKE, Chen S, Luo D, Zhu F. Near-infrared and visible light dual-mode organic photodetectors. *Sci Adv*. 2020;6(5):eaaw8065.

40. Ji CH, Lee SJ, Oh SY. P3HT-based visible-light organic photodetectors using PEI/PAA multilayers as a p-type buffer layer. *RSC Adv*. 2019;9(64):37180-37187.

41. Bao C, Chen Z, Fang Y, et al. Low-noise and large-linear-dynamic-range photodetectors based on hybrid-perovskite thin-single-crystals. *Adv Mater*. 2017;29(39):1703209.

42. Xiong S, Li L, Qin F, et al. Universal strategy to reduce noise current for sensitive organic photodetectors. *ACS Appl Mater Interfaces*. 2017;9(10):9176-9183.

43. Simone G, Dyson MJ, Meskers SCJ, Janssen RAJ, Gelinck GH. Organic photodetectors and their application in large area and flexible image sensors: the role of dark current. *Adv Funct Mater*. 2020;30(20):1904205.

SUPPORTING INFORMATION

Additional supporting information can be found online in the Supporting Information section at the end of this article.